Low-order planar pressure reconstruction of stalled airfoils using Particle Image Velocimetry data

D. W. Carter and B. Ganapathisubramani[a)]
Dept. of Aeronautical & Astronautical Engineering, University of Southampton, Burgess Road, Southampton, UK SO17 1BJ

(Dated: 16 December 2023)

We present planar time-resolved particle image velocimetry (PIV) measurements of flow in the streamwise surface-normal plane of a NACA 0012 airfoil at chord-based Reynolds number $Re_c = 7 \times 10^4$. The angles of attack $\alpha = 13°$ and $15°$ correspond to transient stall and deep stall flow regimes, respectively. A Poisson solver is utilized to reconstruct the instantaneous planar pressure fields from the PIV with satisfactory comparison in the mean pressure compared with dynamically matched Reynolds-Averaged Navier-Stokes (RANS) simulations. Using the proper orthogonal decomposition (POD), a systematic reduced-order reconstruction of the velocity fields and subsequent pressure fields is used to quantify the required number of velocity modes to achieve a desired accuracy in the instantaneous pressure. Further, a Galerkin projection of the Poisson equation onto the POD subspace is used as a framework to identify the relative contribution of each velocity mode on the resulting pressure field via quadratic stochastic estimation (QSE). In both cases, the zeroth mode (corresponding to the mean) is of leading-order importance. In addition, a tendency of the zeroth mode to interact with vortex-shedding modes is identified.

Keywords: Stall, Pressure Reconstruction, POD, Particle Image Velocimetry

I. INTRODUCTION

Enabled by the ever evolving capabilities of image sensors and experimental methodologies, pressure reconstructions from experimental particle image velocimetry (PIV) fields have experienced increasing popularity over the past decade.[1,2] This despite the challenges of such reconstructions, such as the stringent requirements on resolution in space, time, and domain size.[3] These reconstructions offer promising insight on a multitude of engineering problems ranging from fundamental dynamics[4–6] to imparted forces[7–9] to the estimation of far-field noise.[10–12]

In parallel to these advances, the fluid mechanics community has also witnessed a rapid adoption of data-driven techniques for both numerical and experimental data.[13,14] In addition to their use for error mitigation and data refinement,[15–18] these powerful techniques offer a framework to gain a multitude of insights on the flow physics as well.[19] In particular, the proper orthogonal decomposition[20] (POD) is a popular data-driven basis due its inherent property of being energy-optimal and thus retaining as much flow information as possible with a low-rank truncation.[21] Details on the meaning of "low-rank" or "low order" are outlined in section III. Further, the POD itself may be used as a basis to recast the Navier-Stokes equations via a Galerkin projection. This framework is useful for a number of interests, such as stability analysis[22,23] or decreasing computational costs of simulations.[24,25] Recently, Raiola (2022)[26] demonstrated the use of the Galerkin projection to probe the relationship between velocity structures from PIV and the reconstructed pressure fields of a flapping wing on an interaction-by-interaction basis. This framework has the potential to elucidate the role of velocity structures on the resulting pressure fields for a variety of flows of interest.

[a)]Electronic mail: G.Bharath@soton.ac.uk

In the present study, we invoke both advances in pressure-reconstructions and data-driven techniques to understand the relationship between pressure fields and velocity field structures in the flow of a statically stalled airfoil. In particular, we focus on the case of a NACA 0012 in transitional and deep stall at chord-based Reynolds number $Re_c = 7 \times 10^4$. At this Reynolds number the flow is turbulent. As a result, pressure reconstructions are challenging and, due to the multiscale nature of turbulence, the POD is slow to converge. More details on this flow, the data processing, and the POD may be found in a previous publication by the authors.[6]

A large body of work has been dedicated to understanding the nature of static stall for a variety of airfoils. In most cases, these studies focus on pressure measurements to determine the nature of the stall (i.e. thin airfoil stall, leading edge or trailing edge stall[27]) or the influence of external conditions on stall.[28] More recently, PIV has been used for pressure reconstructions to gain insight on the imparted forces. For example, to evaluate the influence of the unsteady pressure on the rotating airfoils of turbine blades[9] or the forces over 2D bodies in incompressible and compressible flows.[8] In these studies, the integral form of the momentum equation is invoked to calculate the lift and drag on the body of interest. The Galerkin framework[26] differs in that the interaction of velocity structures and their contribution to the pressure field (and therefore to the imparted forces) can be evaluated directly: lending valuable insight for the flow of interest.

The goal of the present work is to directly relate the underlying structures of the PIV fields in the stalled airfoil, captured via POD, to the pressure fields reconstructed using a Poisson-solver with appropriate boundary conditions. To achieve this, we will utilize the aforementioned Galerkin framework. Given the widespread adoption of POD in the experimental fluid mechanics community to mitigate noise, a secondary low-hanging fruit is to explore the impact of a simple POD truncation in the velocity fields on the resulting pressure reconstruction. This is because the source term of the pressure reconstruction via the Poisson equation is non-linear in the velocity fields. The POD truncation, which is linear, will therefore have a non-trivial impact on the source term (see equation 1 and discussion in section II). This will be explored as a secondary goal in this work. Details of the data collection and pressure reconstruction methodology are presented in section II. The POD framework used for low-order reconstructions is introduced in section III. The use of a Galerkin projection to gain insight on the underlying mode interactions is presented in IV. Finally, conclusions and directions for future work will be discussed in section V.

II. PIV MEASUREMENTS AND PLANAR PRESSURE RECONSTRUCTION

Data was collected via experiment using stitched time-resolved particle image velocimetry (PIV) in the water flume facility at the University of Southampton. The experiments are discussed in detail in Carter & Ganapathisubramani (2023a,b)[6,12], therefore a brief summary is given here. A vertically oriented NACA 0012 airfoil of chord length $c = 0.15$ m and submerged span $s = 0.43$ m was placed in the mid-span of the flume following the contraction into the test section. For the illumination, a high-speed Nd:YLF laser (Litron 527 nm) operating at 1 kHz was optically directed inwards from either side of the facility and expanded into two overlapping sheets to illuminate the stream-wise surface-normal plane without creating a shadow. Caution was exercised to ensure close overlap between the laser sheets, with a nominal thickness at the flume mid-span of 2 mm. The laser was synchronized to three high-speed Phantom Veo 640-S cameras mounting 105 mm Nikon lenses directed upwards from beneath the facility with overlapping fields of view (FoV). A total of three cameras were used to strike a balance between a large spatial domain but with velocity-gradient-resolving spatial resolution. Both of these features are desirable for quality pressure reconstructions[1,2] that will be explored in this study.

Two cases are presented at fixed angles of attack $\alpha = 13°$ and $\alpha = 15°$. For both cases, the free stream velocity of the facility was set to $U_\infty = 0.5$ m/s corresponding to a chord-based Reynolds number $Re_c = \frac{U_\infty c}{\nu} = 7 \times 10^4$ where ν is the kinematic viscosity. At this

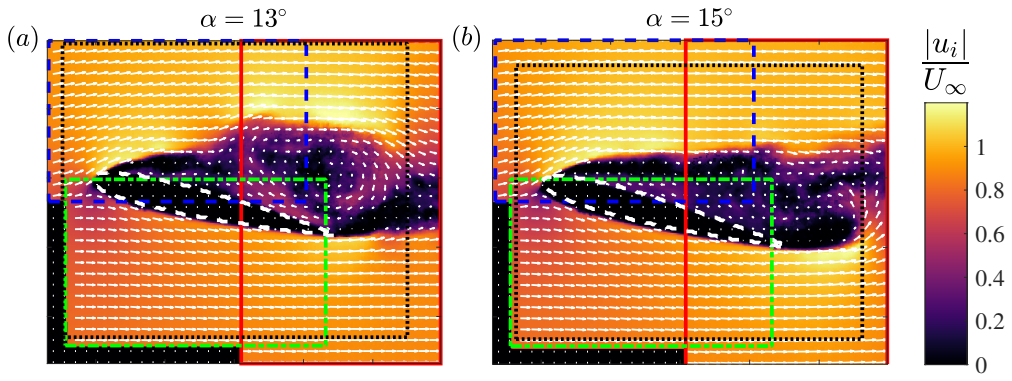

FIG. 1. Instantaneous velocity fields at $\alpha = 13^\circ$ (a) and $\alpha = 15^\circ$ (b) with the airfoil cross section indicated (dashed white). The solid red, dashed blue, and dash-dot green rectangles illustrate the overlapping fields of view from the individual cameras. The dotted rectangle corresponds to the domain used for analysis from each data set. One in every eight PIV vectors are shown.

Reynolds number transitional and deep stall flow regimes were observed for the $\alpha = 13^\circ$ and $\alpha = 15^\circ$ cases, respectively[6]. Two arbitrary snapshots for each case are presented in figure 1. In the figure, a dotted rectangle is used to demarcate the region of the spatial domain that is extracted for each case from the slightly larger stitched PIV fields. These domains are selected by inspection to avoid some edges of the FoVs that are susceptible to weaker signal-to-noise ratio in the PIV[29]. Because the airfoil in the experiment extends downwards towards the upward facing cameras, a small visual occlusion was produced on the pressure side of the airfoil, preventing data collection very close to the surface. This can be seen in figures 1 and 2. The pressure data reported along the surface (figure 2c) is taken from the nearest available grid points.

The instantaneous planar pressure reconstructions were obtained using a Poisson solver approach[1,3]. It begins applying the divergence operation to the Navier-Stokes (NS) momentum equations

$$\nabla^2 p = \boldsymbol{\nabla} \cdot \Big[-\rho\Big(\frac{\partial \boldsymbol{u}}{\partial t} + \boldsymbol{u} \cdot \boldsymbol{\nabla}\boldsymbol{u} - \nu\nabla^2\boldsymbol{u}\Big)\Big] \tag{1}$$

where in this study $\boldsymbol{u}(\boldsymbol{x}, t)$ is the planar instantaneous velocity at positions $\boldsymbol{x}$ and time t, $p(\boldsymbol{x}, t)$ the planar pseudopressure, and ρ the constant fluid density. Note that for incompressible flow (divergence free) the first and last terms on the RHS are identically zero. As a complete reconstruction requires three dimensional information, hereafter the planar pseudopressure is referred to simply as the "pressure". To reconstruct it, two integrations of equation 1 are necessary. The first integration utilizes Neumann boundary conditions on the inlet, outlet, and suction (upper) boundaries of the domain (figure 1). The Neumann boundary conditions are obtained solving for the pressure gradient terms in the NS momentum equations, with gradients calculated via second order differences in space and time. The second integration uses Dirichlet boundary conditions on the pressure (lower) boundary of the domain, where the flow is approximately irrotational and Bernoulli's equation is expected to hold.

The normalized mean pressure fields for both cases are shown in figure 2, where the pressure coefficient is defined as $C_p = P/\frac{1}{2}\rho U_\infty^2$ where P is the ensemble-averaged pressure. To provide comparison for the pressure reconstructions, a dynamically matched Reynolds-averaged Navier-Stokes simulation was conducted using OpenFOAM software. A standard C-type mesh grid was used for the simulation domain and a k-ω SST model for the eddy viscosity. The resulting surface pressure coefficient is shown in figure 2c for both cases with the PIV distributions for comparison. The planar pressure reconstructions yield good agreement in the pressure beyond $x/c \approx 0.25$, but deviate heavily near the leading edge (LE). In

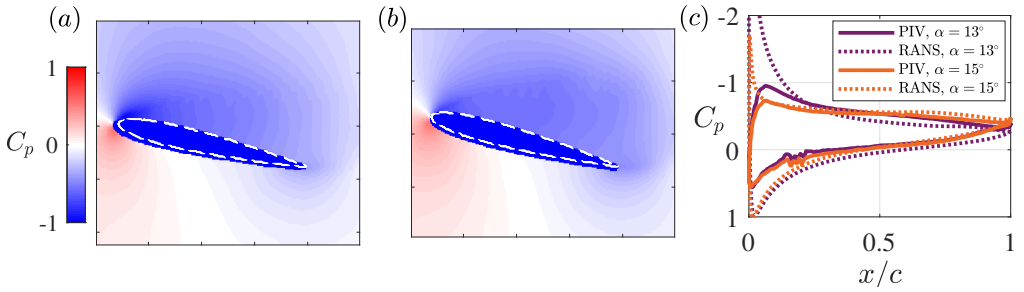

FIG. 2. Pressure coefficient fields for the $\alpha = 13°$ (a) and $\alpha = 15°$ (b) cases. The pressure coefficients at the airfoil surface from the PIV (solid) and dynamically matched RANS simulations (dotted) are plotted for comparison in (c).

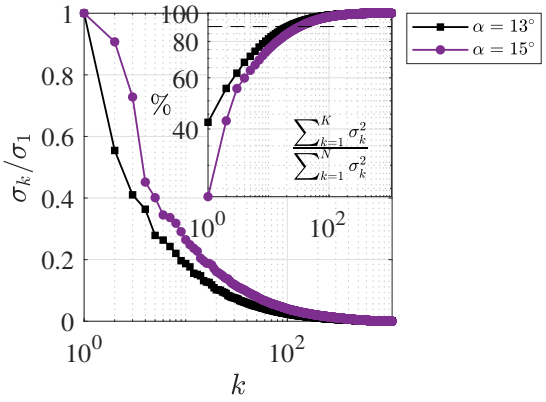

FIG. 3. Singular value spectra for both cases normalized by σ_1, with the cumulative energy distribution inset and a dotted line corresponding to 95% accumulated energy. For reference, the zeroth singular values are $\sigma_0/\sigma_1 = 10.1$ and $\sigma_0/\sigma_1 = 12.4$ for $\alpha = 13°$ and $\alpha = 15°$ respectively.

particular, the LE peak on the suction side is difficult to capture from PIV reconstruction due to the thin boundary layer and confined gradients near the surface. Upon comparison, the pressure reconstructions appear satisfactory for the exploratory purposes of the present study where we desire to probe the effect of a linear decomposition (outlined in the next section) on the resulting non-linear reconstruction via equation 1.

III. LOW-ORDER PRESSURE RECONSTRUCTION VIA PROPER ORTHOGONAL DECOMPOSITION

A low-order representation of the velocity fields is obtained using the proper orthogonal decomposition (POD).[20] POD is commonly employed for data reduction due to its inherent energy optimality.[13] This arises from an eigendecomposition of the velocity autocorrelation used to calculate the POD modes. Using POD, the velocity fields $\boldsymbol{u}(\boldsymbol{x}, t)$ are expressed exactly as

$$\boldsymbol{u}(\boldsymbol{x}, t) = \sum_{k=0}^{N} \psi_k(t)\sigma_k\phi_k(\boldsymbol{x}) \tag{2}$$

where k is the mode number, ψ_k, and ϕ_k are the k-th orthogonal temporal and spatial modes, and σ_k the k-th singular value characterizing the relative contribution of each mode ranked conventionally from highest to lowest. Note here the summation begins at $k = 0$

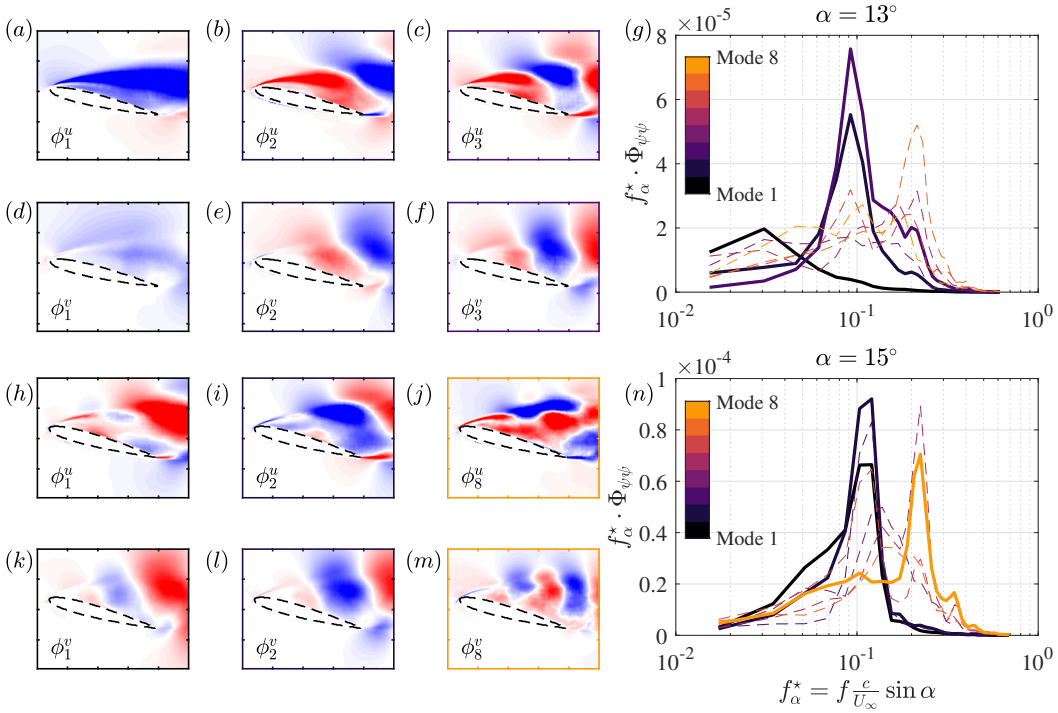

FIG. 4. Three streamwise (a-c,h-j) and cross-stream (d-f,k-m) spatial modes ϕ_k and corresponding pre-multiplied spectra of the first 8 temporal modes (g,n) for $\alpha = 13°$ (a-g) and $\alpha = 15°$ (h-n). The borders of the spatial spectra correspond to the solid lines and colors of panels (g,n). The modes are selected based on their leading contributions to partial pressures discussed in section IV.

and the velocity $\boldsymbol{u}(\boldsymbol{x}, t)$ is the total velocity such that the zeroth mode corresponds to the mean. The total number of snapshots N used to calculate the modes was selected to be $N = 1075$, with snapshots sampled randomly across all runs for both cases. When all possible modes are retained the instantaneous velocity fields via equation 2 are recovered exactly. A low order representation of the velocity $\tilde{\boldsymbol{u}}(\boldsymbol{x}, t)$ can instead be produced by truncating the summation at a selected truncation mode K such that

$$\tilde{\boldsymbol{u}}(\boldsymbol{x}, t) = \sum_{k=0}^{K} \psi_k(t)\sigma_k\phi_k(\boldsymbol{x}). \tag{3}$$

When the singular values decreases rapidly, such as for laminar flows, most of the energy of the velocity fields can be captured in only several modes[14] and truncated at low K. For turbulent flows on the other hand, the singular values decrease gradually due to the inherent multiscale nature of turbulence. This is reflected by the singular values for both cases in figure 3, and necessitated using a large number of snapshots ($N = 1075$) to converge the POD. The inset panel reveals that for both cases approximately 20 modes are required to capture 95% of the fluctuating energy (on the other hand, hundreds of modes are required to capture 99%).

The structures underlying the flow from the spatial modes are plotted in figure 4 (left) with their corresponding pre-multiplied spectra (right). The first two spatial modes (left-most and second-from-left columns) and their corresponding spectra highlight the distinct difference between the two cases. For the case at $\alpha = 13°$, the first spatial mode is uniform in the separated region with a low-frequency peak at $f_\alpha^\star = f\frac{c}{U_\infty}\sin\alpha$ (where f is the frequency in Hz) of $O(10^{-2})$, corresponding to a low-frequency expansion and contraction

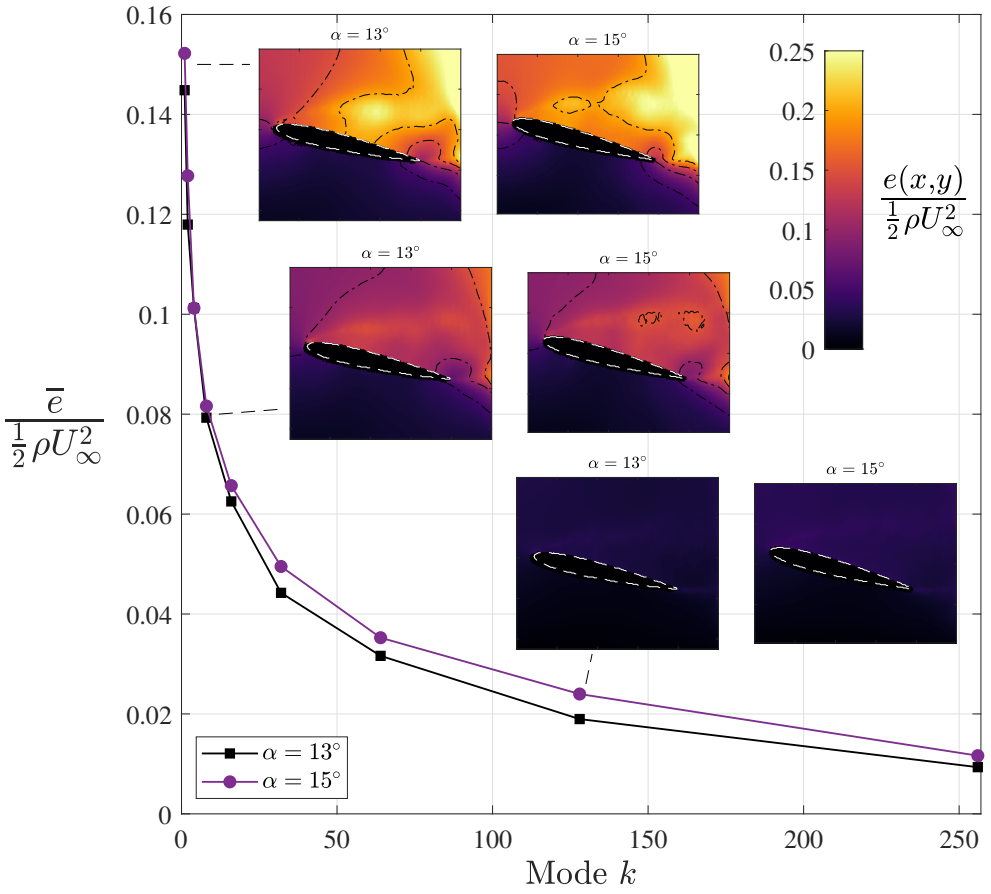

FIG. 5. Spatially averaged reconstruction error $\overline{e}$ between the pressure reconstructed using reduced order velocity modes and the pressure using all modes with increasing number of retained modes. The spatial distributions are shown (inset) for $k = 1$, $k = 8$, and $k = 128$, with contours drawn at $e/\frac{1}{2}\rho U_\infty^2 = [0.05\ 0.1\ 0.15\ 0.2]$.

in a direction approximately normal to the suction side of the airfoil. This is the signature of energetic separation and reattachment events in transitional stall[30]. In contrast, the case at $\alpha = 15°$ shows alternation in the first spatial mode with a frequency peak $f_\alpha^\star$ of $O(10^{-1})$ corresponding to bluff body vortex shedding[31,32] in deep stall.

A natural curiosity that stems from the use of POD is the degree to which a certain truncation impacts the resulting pressure reconstruction. This is because POD is a linear decomposition whereas the source term on the RHS upon the integration of equation 1 is non-linear. This consideration is important for numerous experimental and numerical tools that use POD to analyze flows. For example, POD is commonly used to truncate experimental noise[16,18] or to extend simulations at low computational cost.[33] For the latter, it is necessary to model the pressure term.[34] As a first step, the low-order pressure reconstruction is obtained with increasing K such that

$$\nabla^2 \tilde{p} = \boldsymbol{\nabla} \cdot \Big[-\rho\Big(\frac{\partial \tilde{\boldsymbol{u}}}{\partial t} + \tilde{\boldsymbol{u}} \cdot \boldsymbol{\nabla}\tilde{\boldsymbol{u}} - \nu\nabla^2\tilde{\boldsymbol{u}}\Big)\Big]. \tag{4}$$

The discrepancy between the low-order pressure reconstruction and the "full" order one is quantified as

$$e(\boldsymbol{x}) = \langle |p(\boldsymbol{x}) - \tilde{p}(\boldsymbol{x})| \rangle \tag{5}$$

where the angled brackets denote ensemble averaging across all runs. This is plotted for both cases in figure 5, with similar trends between cases. Here the overbar $\overline{e}$ denotes spatial averaging. A decrease in $\overline{e}$ with increasing retained modes is evident, however the spatial average of the discrepancy is highly dependent on the domain size. The inset plots reveal the average discrepancy in the separated region of the flow specifically is about 0.25 times the free-stream dynamic pressure ($P_{dyn} = \frac{1}{2}\rho U_\infty^2$) with just one fluctuating mode and decreases to 0.1 with 8 modes. As expected, the discrepancy decreases non-monotonically with increasing number of retained modes. The difference between the cases is slight, with larger average discrepancy in the deep stall cases compared to the transitional stall case.

As a first approach, the low-order pressure reconstructions quantify the required number of velocity modes to achieve similarity to the full-order reconstruction. This analysis however does not reveal the role of the modes individually on the resulting pressure. This is investigated in detail in the following section.

IV. MODE PAIR CONTRIBUTIONS VIA GALERKIN PROJECTION

To elucidate the underlying interactions within the velocity fields giving rise to the instantaneous pressure, a Galerkin projection of the pressure Poisson equation is performed onto the basis spanned by the POD:[21,26]

$$\nabla^2 p = -\rho \sum_{i=0}^{N} \sum_{j=0}^{N} \psi_i(t)\psi_j(t)\sigma_i\sigma_j Q_{i,j} \tag{6}$$

where $Q_{i,j}(\boldsymbol{x}) = \boldsymbol{\nabla}\cdot(\phi_i(\boldsymbol{x})\cdot\boldsymbol{\nabla})\phi_j(\boldsymbol{x})$ arises from the i-th and j-th interacting spatial modes. The solution may be expressed in terms of the sum over the interactions as

$$p(\boldsymbol{x},t) = \sum_{i=0}^{N} \sum_{j=0}^{N} \psi_i(t)\psi_j(t)\hat{p}_{i,j}(\boldsymbol{x}) \tag{7}$$

where $\hat{p}_{i,j}(\boldsymbol{x})$ is known as the partial pressure.[34] The partial pressure reveals the combinations of velocity modes that give rise to a particular structure in the pressure field. To quantify the contribution of each partial pressure we decompose them such that

$$\hat{p}_{i,j}(\boldsymbol{x},t) = \sigma^p_{i,j}\check{p}_{i,j}(\boldsymbol{x}) \tag{8}$$

where $\sigma^p_{i,j}$ is the magnitude of the partial pressure and $\check{p}_{i,j}(\boldsymbol{x})$ is the spatial distribution of each partial pressure with unit norm.

With the Galerkin framework established, all that remains is to calculate the partial pressures by solving equation 6 for each velocity mode combination. This approach is problematic for two reasons. Firstly, since in the present study $N = 1075$ modes, there will be 1.16×10^6 integrations required to include all mode combinations: a number that is prohibitively large. It is clear that only a subset of mode combinations can be feasibly studied. The second problem is that each integration requires restating the non-homogeneous boundary conditions.[34] Though methods have been developed for numerical simulations to overcome this difficulty,[33,35] the influence of experimental noise adds additional complexity.

The alternative to integrating equation 6 is to instead leverage the fact that the pressure fields and the temporal velocity modes are known quantities. It is therefore possible to use a stochastic estimation technique to recover the partial pressures[36]. In particular, following Raoila (2022), due to the quadratic non-linearity of the convective terms we utilize quadratic stochastic estimation (QSE) to estimate the partial pressures.[26,37] The method consists of constructing two matrices $\boldsymbol{W}$ and $\boldsymbol{V}$ such that

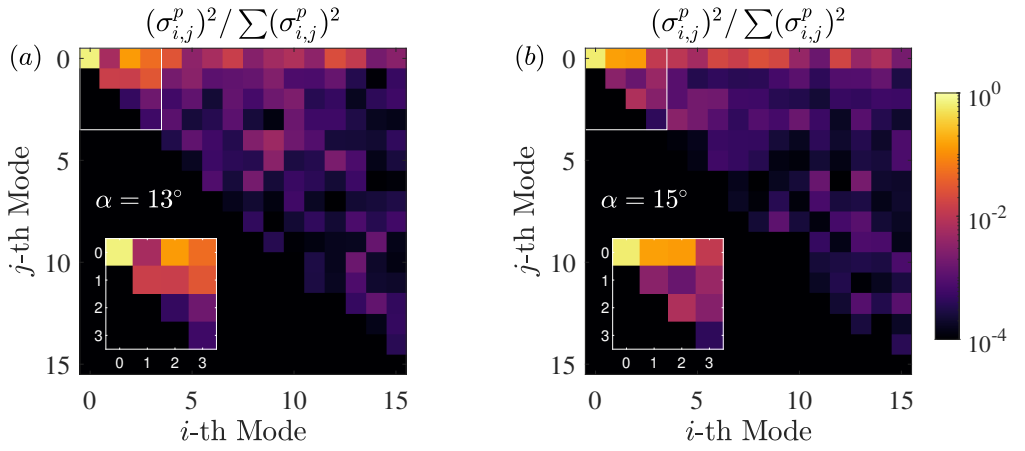

FIG. 6. Relative contribution of the partial pressures for velocity mode combinations for $\alpha = 13°$ (a) and $\alpha = 15°$ (b). The combinations are symmetric about the diagonal, and only the upper triangle is plotted. A zoom of the first four interactions is also shown (inset).

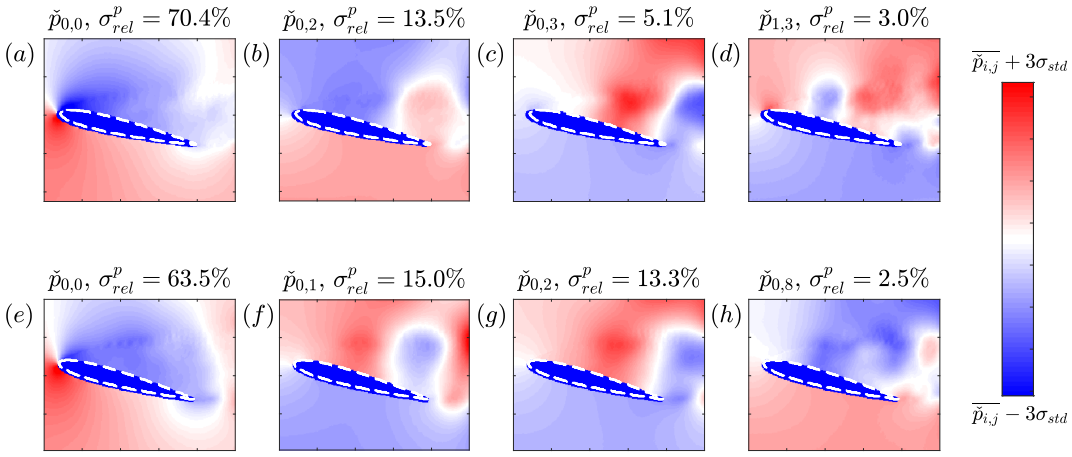

FIG. 7. Partial pressure fields of the leading four interactions for $\alpha = 13°$ (a-d) and $\alpha = 15°$ (e-f). Colorbars are normalized by plus or minus three standards deviations from the spatial mean of each partial pressure.

$$\underbrace{\begin{bmatrix} \langle \psi_1\psi_1, \psi_1\psi_1 \rangle & \dots & \langle \psi_K\psi_K, \psi_1\psi_1 \rangle \\ \vdots & \ddots & \vdots \\ \langle \psi_1\psi_1, \psi_K\psi_K \rangle & \dots & \langle \psi_K\psi_K, \psi_K\psi_K \rangle \end{bmatrix}}_{\boldsymbol{W}} \underbrace{\begin{bmatrix} \hat{p}_{1,1} \\ \vdots \\ \hat{p}_{K,K} \end{bmatrix}}_{\tilde{\boldsymbol{P}}} = \underbrace{\begin{bmatrix} \langle p, \psi_1\psi_1 \rangle \\ \vdots \\ \langle p, \psi_K\psi_K \rangle \end{bmatrix}}_{\boldsymbol{V}} \tag{9}$$

where here the angled brackets with a comma $\langle \cdot, \cdot \rangle$ denote the inner product, $\tilde{\boldsymbol{P}}$ is the matrix of partial pressures and K is again the truncated number of modes leading to $I = K^2$ interactions. The solution is given simply as $\tilde{\boldsymbol{P}} = \boldsymbol{W}^{-1}\boldsymbol{V}$, however the matrix $\boldsymbol{W}$ is poorly conditioned and therefore a pseudoinverse is necessary to prevent the solution from diverging i.e. $\tilde{\boldsymbol{P}} = \boldsymbol{W}^{\dagger}\boldsymbol{V}$. In addition, we select $K = 16$ modes ($I = 256$) for the QSE analysis. More details regarding the treatment of the matrix $\boldsymbol{W}$ and the sensitivity to the number of interactions can be found in appendix A.

The relative contribution of each partial pressure captured by the magnitude $\sigma^p_{i,j}$ is shown in figure 6 normalized by the sum across all interactions. In expected fashion, the dom-

inant contribution to the pressure (noting the logarithmic scale) originates from the $\check{p}_{0,0}$ interactions corresponding to the mean velocity modes and resulting mean pressure. In addition, the sub-leading interactions are consistent across cases in that interactions of low-order modes with the zeroth mode are seen to be sub-leading. The reader is referred to figure 4 to visualize the spatial shape and temporal characteristics of the sub-leading interacting modes. These leading-order linear interactions are consistent with a linear approximation for the unresolved Galerkin expansion coefficients in numerical simulations, e.g. from Galetti *et al.* (2004)[38] in a wake flow model.

The spatial contribution of each partial pressure is visualized in figure 7 for the leading four interactions in both cases. Note that the sign (positive or negative) of the partial pressures is arbitrary due to the arbitrary sign of the temporal modes (equation 7). A striking resemblance is seen in the first three interactions across cases, both in terms of their relative contribution (where $\sigma^p_{rel} = \sigma^p_{i,j} / \sum_{i=0}^{K} \sum_{j=0}^{K} \sigma^p_{i,j}$) as well as their structure. Examination of the velocity modes and their spectra in figure 4 reveals in both cases the sub-leading modes correspond to bluff body vortex shedding. Note, these modes are interacting with the (time constant) zero-th mode corresponding to the mean velocity.

Beyond the first three leading interactions, the partial pressures are seen to differ between cases. In transitional stall, the fourth leading interaction is non-linear between the first and third velocity modes. Recalling that the first velocity mode at $\alpha = 13°$ peaks at low frequencies related to separation and reattachment, such an interaction is not expected to be seen in the deep stall case as the flow never reattaches. Indeed, the fourth leading interaction in the deep stall case is a linear interaction between the zero-th and eighth modes, corresponding to a shear layer flapping frequency and structure.

V. CONCLUSIONS

We have presented an analysis of low-order pressure reconstructions in the flow of static stalled NACA 0012 airfoils at angles of attack corresponding to transitional and deep stall turbulent flow regimes. The focus of this study is two fold. First, to quantify the impact of a low-dimensional representation of the velocity field via POD on the resulting planar pressure reconstructions. Second, to understand the influence of interacting velocity modes on the dynamics of airfoils in transitional and deep stall, with implications for the forces experienced by the body. Such considerations are important as POD is often used as a tool to remove experimental noise.[16–18] To this end, a mode-by-mode framework using a Galerkin projection onto the basis spanned by the POD was utilized. Importantly, this is demonstrated without the need to integrate for each mode interaction, but instead using the data-driven QSE approach.[26]

We find that despite the differences in the transitional and deep-stall cases, namely the low-frequency separation and reattachment in the transitional case, the leading and sub-leading interactions between the two cases are strikingly similar. The former is attributed to the mean velocity modes themselves. The latter are between the mean and fluctuating structures with peak frequencies in the bluff-body vortex shedding regime. The linear nature of the leading sub-interactions is consistent with Galerkin models in the computational fluid dynamics literature.[34,38]

This present work has demonstrated the utility of a Galerkin framework applied to experimental data to elucidate the nature of the underlying interactions in the velocity fields and their contribution to the instantaneous pressure. Following Raoila (2022), this was achieved via the QSE[26] in a fully turbulent flow obtained via experiment. Provided that the POD is satisfactorily converged, our work indicates that, for the present advective turbulent flow, the primary contributions to the pressure are captured by interactions in the first eight modes. These interactions account for 89% and 92% of the instantaneous pressure fields (in terms of the relative magnitude of the partial pressures) for the transitional and deep stalled cases, respectively.

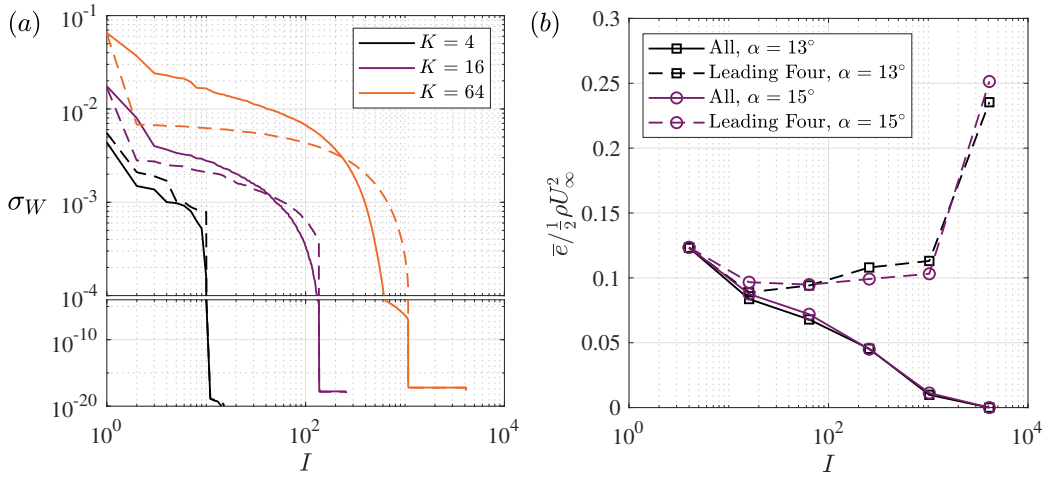

FIG. 8. Singular values of the matrix $\boldsymbol{W}$ central to the QSE implementation (section IV) for the case at $\alpha = 15°$ plotted against the total number of interactions (a) (similar results for $\alpha = 13°$ omitted for brevity). The dashed lines correspond to singular values using synthetic Gaussian random temporal modes. The reconstruction discrepancy (b) is shown for both cases using all interactions (solid) and using only the leading four interactions (dashed).

ACKNOWLEDGMENTS

The authors are grateful for financial support from the Engineering and Physical Sciences Research Council (Ref No: EP/R010900/1) and H2020 Future and Emerging Technologies Project HOMER 769237.

DATA AVAILABILITY

All data presented in this study has been used in previous work and is openly available from the University of Southampton repository at `http://dx.doi.org/10.5258/SOTON/D2466`

Appendix A: Treatment of the matrix $\boldsymbol{W}$

In order to recover the partial pressures, it is necessary to invert the matrix $\boldsymbol{W}$ as defined in equation 9. In the present framework, every temporal mode (except the zero-th) is a fluctuating quantity with zero-mean. As a result, uncorrelated inner products are vanishingly small and inevitably leads to a poorly conditioned $\boldsymbol{W}$, i.e. the ratio of the maximum and minimum singular values $\sigma_{W,max}/\sigma_{W,min} \to \infty$. This is demonstrated in figure 8a for both data in the deep stall case and for a synthetic matrix constructed from Gaussian randomly distributed temporal modes (dashed). The random distributions are provided to demonstrate that the poor conditioning is inherent to the construction of $\boldsymbol{W}$ and not caused by experimental noise.

An important choice for constructing $\boldsymbol{W}$ is the number of modes K (and therefore number of interactions I) to consider. As can be inferred from figure 8a, as K increases $\boldsymbol{W}$ is increasingly poorly conditioned. A secondary consideration is that increasing K corresponds to a quadratic increase in computational expense. Finally, with increasing interactions the role of bias error in the PIV (due to sub-pixel limitations) is increasingly prevalent within each inner product of equation 9, and this self-correlating noise pollutes the singular values. This can be seen in figure 8b, which plots the reconstruction discrepancy between the pressure

and the QSE reconstruction via equation 7. The leading four interactions (dashed lines), which are expected to plateau beyond several considered interactions, suddenly experience massive reconstruction discrepancy beyond a certain number of interactions. This is the signature of these self-correlating noise corrupting the singular values of $\boldsymbol{W}$.

For the present study, we opt to consider $K = 16$ modes to strike a balance between a large number of interactions ($I = 256$), low computational cost, and avoiding self-correlating noise artifacts. A pseudo-inverse is employed to treat the poorly conditioned $\boldsymbol{W}$. We note that for the present data sets the results were similar in the range $4 < K < 32$, with differences (e.g. relative contribution and structure of the partial pressures) on the order of a few percent.

[1]R. De Kat and B. Van Oudheusden, "Instantaneous planar pressure determination from PIV in turbulent flow," Experiments in fluids **52**, 1089–1106 (2012).
[2]P. Van Gent, D. Michaelis, B. Van Oudheusden, P.-É. Weiss, R. de Kat, A. Laskari, Y. J. Jeon, L. David, D. Schanz, F. Huhn, *et al.*, "Comparative assessment of pressure field reconstructions from particle image velocimetry measurements and lagrangian particle tracking," Experiments in Fluids **58**, 1–23 (2017).
[3]A. Laskari, R. de Kat, and B. Ganapathisubramani, "Full-field pressure from snapshot and time-resolved volumetric PIV," Experiments in fluids **57**, 1–14 (2016).
[4]J. Lawson and J. Dawson, "On velocity gradient dynamics and turbulent structure," Journal of Fluid Mechanics **780**, 60–98 (2015).
[5]A. N. Knutsen, P. Baj, J. M. Lawson, E. Bodenschatz, J. R. Dawson, and N. A. Worth, "The inter-scale energy budget in a von kármán mixing flow," Journal of Fluid Mechanics **895** (2020).
[6]D. W. Carter and B. Ganapathisubramani, "Low-order modeling and sensor-based prediction of stalled airfoils at moderate reynolds number," AIAA Journal , 1–13 (2023).
[7]N. Fujisawa, S. Tanahashi, and K. Srinivas, "Evaluation of pressure field and fluid forces on a circular cylinder with and without rotational oscillation using velocity data from PIV measurement," Measurement Science and Technology **16**, 989 (2005).
[8]B. W. Van Oudheusden, F. Scarano, E. W. Roosenboom, E. W. Casimiri, and L. J. Souverein, "Evaluation of integral forces and pressure fields from planar velocimetry data for incompressible and compressible flows," Experiments in fluids **43**, 153–162 (2007).
[9]A. Villegas and F. Diez, "Evaluation of unsteady pressure fields and forces in rotating airfoils from time-resolved PIV," Experiments in Fluids **55**, 1–17 (2014).
[10]V. Koschatzky, J. Westerweel, and B. Boersma, "A study on the application of two different acoustic analogies to experimental PIV data," Physics of Fluids **23**, 065112 (2011).
[11]V. Lorenzoni, M. Tuinstra, and F. Scarano, "On the use of time-resolved particle image velocimetry for the investigation of rod–airfoil aeroacoustics," Journal of Sound and Vibration **331**, 5012–5027 (2012).
[12]D. W. Carter and B. Ganapathisubramani, "Data-driven determination of low-frequency dipole noise mechanisms in stalled airfoils," Experiments in Fluids **64**, 41 (2023).
[13]K. Taira, S. L. Brunton, S. T. Dawson, C. W. Rowley, T. Colonius, B. J. McKeon, O. T. Schmidt, S. Gordeyev, V. Theofilis, and L. S. Ukeiley, "Modal analysis of fluid flows: An overview," Aiaa Journal **55**, 4013–4041 (2017).
[14]K. Taira, M. S. Hemati, S. L. Brunton, Y. Sun, K. Duraisamy, S. Bagheri, S. T. Dawson, and C.-A. Yeh, "Modal analysis of fluid flows: Applications and outlook," AIAA journal **58**, 998–1022 (2020).
[15]N. E. Murray and L. S. Ukeiley, "An application of gappy pod," Experiments in Fluids **42**, 79–91 (2007).
[16]S. G. Raben, J. J. Charonko, and P. P. Vlachos, "Adaptive gappy proper orthogonal decomposition for particle image velocimetry data reconstruction," Measurement Science and Technology **23**, 025303 (2012).
[17]M. Mendez, M. Raiola, A. Masullo, S. Discetti, A. Ianiro, R. Theunissen, and J.-M. Buchlin, "Pod-based background removal for particle image velocimetry," Experimental Thermal and Fluid Science **80**, 181–192 (2017).
[18]I. Scherl, B. Strom, J. K. Shang, O. Williams, B. L. Polagye, and S. L. Brunton, "Robust principal component analysis for modal decomposition of corrupt fluid flows," Physical Review Fluids **5**, 054401 (2020).
[19]P. J. Schmid, "Dynamic mode decomposition of numerical and experimental data," Journal of fluid mechanics **656**, 5–28 (2010).
[20]G. Berkooz, P. Holmes, and J. L. Lumley, "The proper orthogonal decomposition in the analysis of turbulent flows," Annual review of fluid mechanics **25**, 539–575 (1993).
[21]D. Rempfer and H. F. Fasel, "Evolution of three-dimensional coherent structures in a flat-plate boundary layer," Journal of Fluid Mechanics **260**, 351–375 (1994).
[22]A. Deane, I. Kevrekidis, G. E. Karniadakis, and S. Orszag, "Low-dimensional models for complex geometry flows: application to grooved channels and circular cylinders," Physics of Fluids A: Fluid Dynamics **3**, 2337–2354 (1991).
[23]D. Rempfer, "Low-dimensional modeling and numerical simulation of transition in simple shear flows," Annual review of fluid mechanics **35**, 229 (2003).
[24]M. Balajewicz and E. H. Dowell, "Stabilization of projection-based reduced order models of the navier–stokes," Nonlinear Dynamics **70**, 1619–1632 (2012).

[25]J. S. Hesthaven, G. Rozza, B. Stamm, *et al.*, *Certified reduced basis methods for parametrized partial differential equations*, Vol. 590 (Springer, 2016).
[26]M. Raiola, "Pressure and velocity fields decomposition around a flapping wing," in *Proceedings of the 20th International Symposium on the Application of Laser and Imaging Techniques to Fluid Mechanics, Lisbon, Portugal* (2022).
[27]G. B. Mccullough and D. E. Gault, "Examples of three representative types of airfoil-section stall at low speed," Tech. Rep. (1951).
[28]K. E. Swalwell, J. Sheridan, W. Melbourne, *et al.*, "The effect of turbulence intensity on stall of the naca 0021 aerofoil," in *14th Australasian fluid mechanics conference* (2001) pp. 941–944.
[29]R. J. Adrian and J. Westerweel, *Particle image velocimetry*, 30 (Cambridge university press, 2011).
[30]K. Zaman, D. McKinzie, and C. Rumsey, "A natural low-frequency oscillation of the flow over an airfoil near stalling conditions," Journal of Fluid Mechanics **202**, 403–442 (1989).
[31]S. Yarusevych, P. E. Sullivan, and J. G. Kawall, "On vortex shedding from an airfoil in low-reynolds-number flows," Journal of Fluid Mechanics **632**, 245–271 (2009).
[32]J. Derakhshandeh and M. M. Alam, "A review of bluff body wakes," Ocean Engineering **182**, 475–488 (2019).
[33]S. Hijazi, G. Stabile, A. Mola, and G. Rozza, "Data-driven pod-galerkin reduced order model for turbulent flows," Journal of Computational Physics **416**, 109513 (2020).
[34]B. R. Noack, P. Papas, and P. A. Monkewitz, "The need for a pressure-term representation in empirical galerkin models of incompressible shear flows," Journal of Fluid Mechanics **523**, 339–365 (2005).
[35]S. Lorenzi, A. Cammi, L. Luzzi, and G. Rozza, "Pod-galerkin method for finite volume approximation of navier–stokes and rans equations," Computer Methods in Applied Mechanics and Engineering **311**, 151–179 (2016).
[36]R. J. Adrian, "Stochastic estimation of conditional structure: a review," Applied scientific research **53**, 291–303 (1994).
[37]N. E. Murray and L. S. Ukeiley, "Estimation of the flowfield from surface pressure measurements in an open cavity," AIAA journal **41**, 969–972 (2003).
[38]B. Galletti, C. Bruneau, L. Zannetti, and A. Iollo, "Low-order modelling of laminar flow regimes past a confined square cylinder," Journal of Fluid Mechanics **503**, 161–170 (2004).
[39]A. Caiazzo, T. Iliescu, V. John, and S. Schyschlowa, "A numerical investigation of velocity–pressure reduced order models for incompressible flows," Journal of Computational Physics **259**, 598–616 (2014).
[40]K. Kean and M. Schneier, "Error analysis of supremizer pressure recovery for pod based reduced-order models of the time-dependent navier–stokes equations," SIAM Journal on Numerical Analysis **58**, 2235–2264 (2020).
[41]J. Novo and S. Rubino, "Error analysis of proper orthogonal decomposition stabilized methods for incompressible flows," SIAM Journal on Numerical Analysis **59**, 334–369 (2021).
[42]I. Akhtar, A. H. Nayfeh, and C. J. Ribbens, "On the stability and extension of reduced-order galerkin models in incompressible flows," Theoretical and Computational Fluid Dynamics **23**, 213–237 (2009).
[43]M. J. Balajewicz, E. H. Dowell, and B. R. Noack, "Low-dimensional modelling of high-reynolds-number shear flows incorporating constraints from the navier–stokes equation," Journal of Fluid Mechanics **729**, 285–308 (2013).